Supplementary Information (SI) for Chemical Science.
This journal is © The Royal Society of Chemistry 2024

Supplementary Information

Resolving Molecular Frontier Orbitals in Molecular Junctions with kHz Resolution

Yuji Isshiki[1], Enrique Montes[2], Tomoaki Nishino[1], Héctor Vázquez[2] and Shintaro Fujii[1*]*

[1]Department of Chemistry, School of Science, Tokyo Institute of Technology, 2-12-1 W4-10 Ookayama, Meguro-ku, Tokyo 152-8551, Japan

[2] Institute of Physics, Czech Academy of Sciences, Cukrovarnická 10, Prague, CZ-162 00, Czech Republic

Table of contents

1. Details of measurement system

Measurement system:

We constructed a data acquisition system based on the field programmable gate array (FPGA) device with six output signals and one input signal (Fig. S1): four control voltages for the stepping motors (V_{SM}) operating at tens of nm scale, a voltage (V_{PB}) for piezoelectric devices operating at pm scale, and a voltage (V_{SB}) for current measurement applied between the Au tip and the Au electrode. The output signals are transferred from the FPGA device (PCIe-7852, NI) to a signal access module III (Bruker, Santa Barbara, CA) and applied to each element. The piezo voltage is amplified by a factor of 10 by a piezo driver (E-663, Physik Instrumente) and applied. The input signal is amplified by a SR570 current amplifier (Stanford Research Systems). Four 16-bit integer values of I_{TC}, V_{SB}, V_{PB}, and number of traces (N_{tr}) were integrated into a single 64-bit integer value, which is transferred to LabVIEW user interface using the fast-in fast-out (FIFO) method.

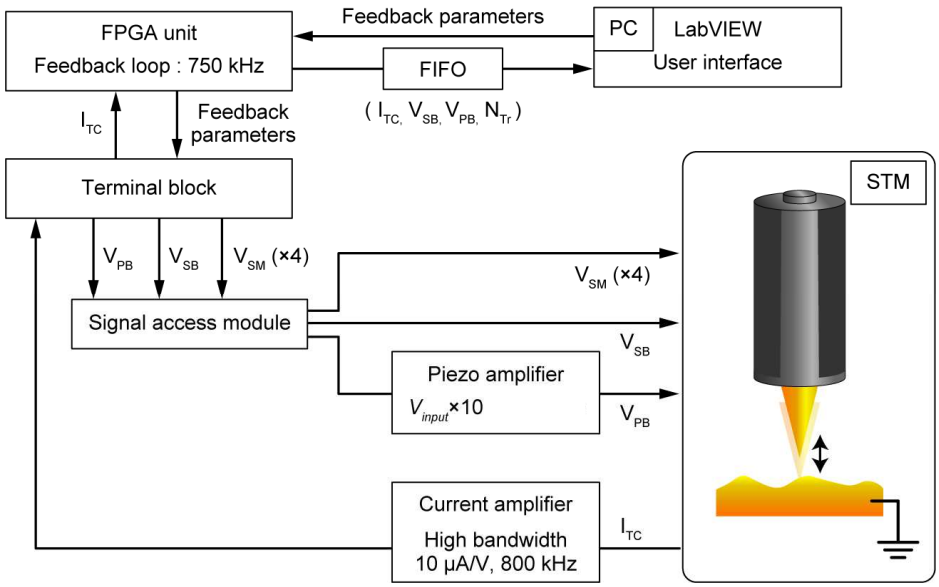

Fig. S1. Overview of *I*–*V* measurement system. I_{TC}, V_{SB}, V_{PB} and N_{tr} indicate the 16-bit integer values of tunnelling current through junctions, sample bias, piezo bias and trace number respectively. V_{SM} shows bias voltage for the step motor of scanning tunnelling microscopy (STM).

Break junction method:

Prior to the *I–V* measurement (Fig. 1a), a Au tip of scanning tunnelling microscopy (STM) was placed in point contact with a Au substrate covered with the target molecules. The STM tip was then moved away from the substrate and the current flowing in the point contact is monitored at a constant bias voltage of 0.05 V. When the conductance of the point contact ($G = I/V$) falls below 10 G_0 ($G_0 = 2e^2/h$,), the application of sinusoidal voltage is started and the point contact is gradually extended with a tip displacement velocity of 1 nm/s (Fig. S3). This elongation broke the point contact and formed a nanogap between the Au substrate and the Au tip. When the conductance falls below 0.8 G_0 and a single molecule was trapped in this nanogap and a single molecule junction was formed, the tip was further moved away from the substrate with a tip displacement velocity of 20 nm/s and the *I–V* measurement in the junction stretching process was continued until the single-molecule junction was broken.

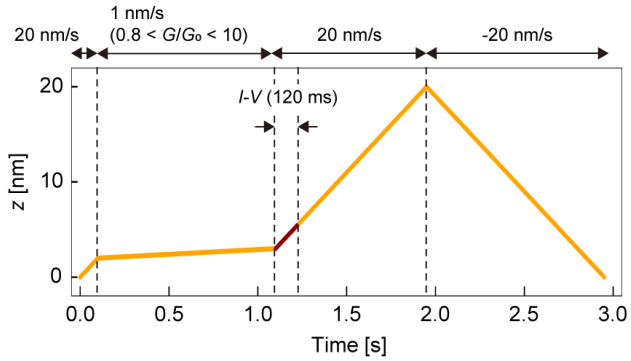

Fig. S2. Piezo displacement in STM-based break junction. Red line is the region of *I–V* measurement.

2. Frequency response of the measurement system

The frequency response and distortion characteristics of the current amplifier used for the electronic measurement were tested as follows. A shunt resistor of 100 k, 1 M, and 10 MΩ was placed between the STM tip folder and the STM stage, and a voltage with frequency ranges from 1 k to 200 kHz was applied. The frequency dependence of gain of the current amplifier was evaluated by applying a sinusoidal voltage of an amplitude of 1.0 V to the shunt resistor. The half value of the wave period (WP) is the time required to measure a single *I*–*V* curve. The frequency dependence was checked by measuring current gain = G / G_{ideal} where G and G_{ideal} are measured and the actual conductance of the shunt resistors (Fig. S2 and Table S1). In the voltage range of −1.0~+1.0 V, the time resolution of the *I*–*V* measurement was up to 5 kHz (WP / 2 = 0.1 ms) if 3 % error is allowed.

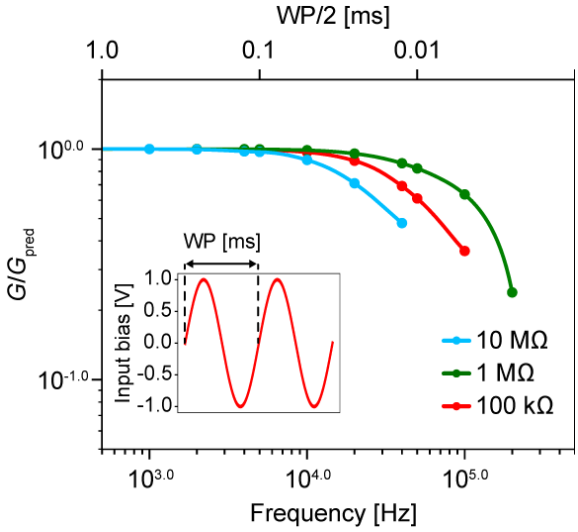

Fig. S3. Frequency dependence of current gain evaluated in terms of sinusoidal voltages with an amplitude of 1.0 V. Insets of (a) and (b) indicate the waveform of applied voltage. The green, red, and light blue data points correspond to the results for the 100 kΩ, 1 MΩ, and 10 MΩ resistors, respectively. G and G_{ideal} correspond to the measured and actual conductance of the shunt resistors.

[a]Period (Frequency) / Resistance	1000 μs (1.00 kHz)	500 μs (2.00 kHz)	250 μs (4.00 kHz)	200 μs (5.00 kHz)	100 μs (10.0 kHz)	50 μs (20.0 kHz)
10 MΩ	1.00	1.00	0.98	0.97	0.90	0.71
1 MΩ	1.00	1.00	1.00	1.00	0.99	0.96
100 kΩ	1.00	1.00	1.00	0.99	0.97	0.89

Period (Frequency) / Resistance	25 μs (40.0 kHz)	20 μs (50.0 kHz)	10 μs (100 kHz)
10 MΩ	0.48	N/A	N/A
1 MΩ	0.87	0.82	0.64
100 kΩ	0.69	0.61	0.36

Table S1. List of gains for a sigmoidal wave with the amplitude of 1.0 V. [a]Period of measuring an *I*–*V* curve corresponds to half the period of the sine wave.

3. *I–V* measurement and analysis

We have reported detailed controlled measurements of Au atomic contacts in a previous study (see ref [38] in the main text). In that study, we investigated the structural asymmetry of single metal-atom contacts using fast *I–V* measurements with a time resolution of about 100 μs, similar to the method employed in this study. the results of these controlled experiments, accompanied by extensive statistical analysis of over 300,000 *I–V* curves, demonstrate the robustness and reliability of our measurement approach. The results demonstrate the robustness and reliability of our measurement approach.

Time course of current measurement for BDI, BPY, BDT, and C_{60}:

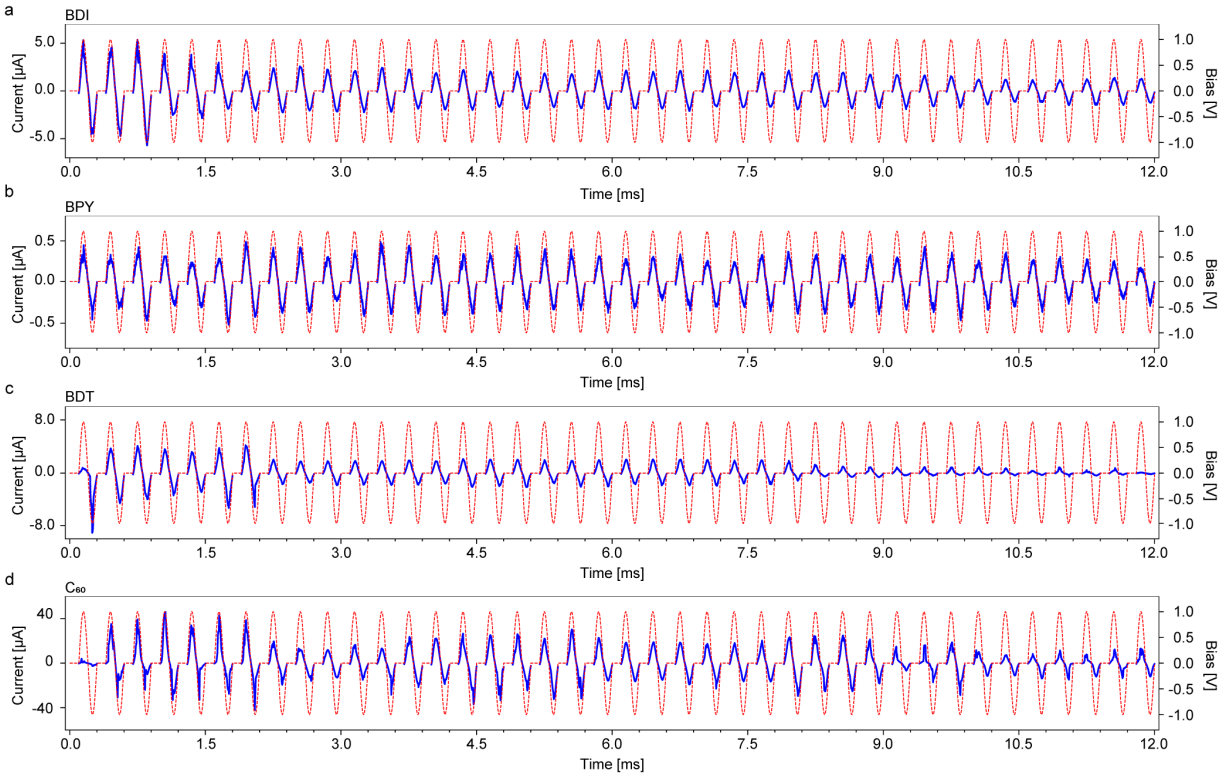

Fig. S4. Time course of *I–V* measurement in Fig. 1d. Blue solid lines and red dashed lines indicate time course of *I–V* curves and applied bias voltage for (a) BPI, (b) BPY, (c) BDT and (d) C_{60}. The time is set to 0 when the single-molecule junction is formed.

Fitting procedure of *I–V* curves:

Several *I–V* curves displayed kinked shapes (*i.e.*, 4.7, 4.3, 13.8 and 9.2 % for BPY, BDI, BDT and C_{60}). Such *I–V* curves were automatically removed from the dataset used for the statistical analysis (Fig. 1d and Fig. 4) because the kinked behaviour must be owing to a major dynamic structural instability of the junction during a single *I–V* measurement cycle [33]. To

remove the kinked *I*–*V* curves (green curves in Fig. S4), a parameter R^2 is defined for each *I*–*V* curve as follows equation (S1):

$$R^2 = \frac{\sum_{i=0}^{N}(I_i - f_i)^2}{\sum_{i=0}^{N}\left(I_i - \overline{I}\right)^2} \quad \text{(S1)}$$

where I_i and f_i are the measured and theoretical currents for the i^{th} data point of the *I*–*V* curve. The theoretical current is obtained by the resonant level model of equation (1), and $\overline{I}$ is the average of current values for each *I*–*V* curve. The kinked *I*–*V* curves with $R^2 > 0.5$ were removed from the dataset (Fig. 1d and Fig. 4). Examples of the removed *I*–*V* curves are shown in green in Fig. S5. Moreover, *I*–*V* curves with $\alpha < 0.1$ and $0.9 < \alpha$ are also removed from the dataset because the *I*–*V* curves of junctions without molecules indicates α values close to 0.0 or 1.0. Definition and dataset of α in Fig. 1d are shown in Fig. S5.

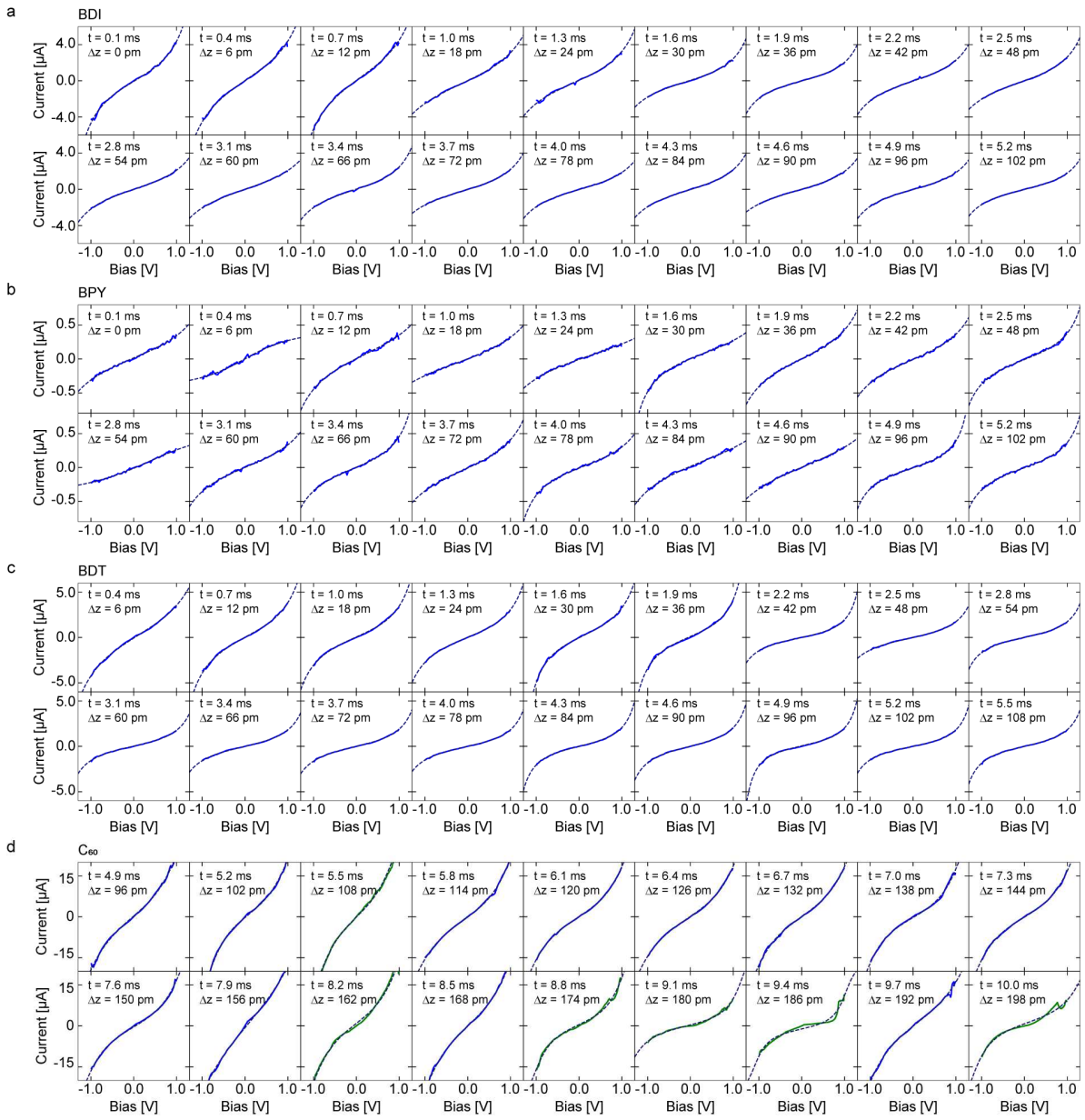

Fig. S5. Fitted results of $I-V$ curves. Solid and dashed lines indicate experimental current and fitted results for $I-V$ curves for (a) BDI, (b) BPY, (c) BDT and (d) C_{60} shown in Fig. 1 taken at 0.3 ms intervals.

α Values during junction stretching:

Symmetry of the $I-V$ curve, α, is defined as $\alpha = \Gamma_R/(\Gamma_R+\Gamma_L)$ where Γ_R and Γ_L corresponds to the meta-molecule electronic coupling for the tip and substrate sides, and $\Gamma = \Gamma_R+\Gamma_L$ (see also equation (1)) [21, 23]. When $\alpha = 0.5$, the metal-molecule electronic couplings of the junction are symmetric ($\Gamma_R=\Gamma_L$), and when $\alpha > 0.5$ ($\alpha < 0.5$), coupling of the tip (substrate) side is higher than that of the substrate (tip) side.

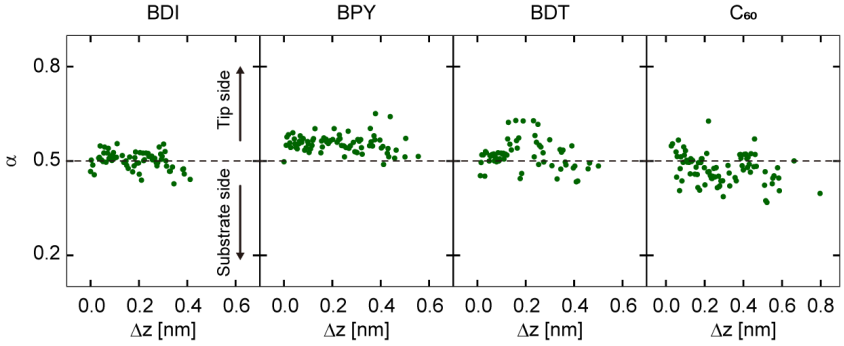

Fig. S6. α values as a function of junction stretching distance (Δz) for BDI, BPY, BDT and C_{60}.

	BDI(H)	BPY(H)	C_{60}(H)	C_{60}(T)	C_{60}(L)	BDT(H)	BDT(M)
$\partial \log G/\partial z$ [nm^{-1}]	−2.52	−1.17	−3.63	−8.43	−3.09	−2.81	−2.31
$\partial \varepsilon/\partial z$ [nm^{-1}]	−0.49	−0.44	1.67	−0.98	0.96	0.87	0.63
$\partial \log \Gamma/\partial z$ [nm^{-1}]	−1.56	−0.84	−0.78	−4.91	−1.31	−1.92	−2.01

Table S2. $\partial \log G/\partial z$, $\partial \varepsilon/\partial z$, and $\partial \log \Gamma/\partial z$ along with junction elongation for BPY, BDI, C_{60} and BDT in Fig. 1d.

***G*, *ε*, *Γ*, and AF *vs*. Δ*z* traces for BDI, BPY, BDT and C_{60}:**

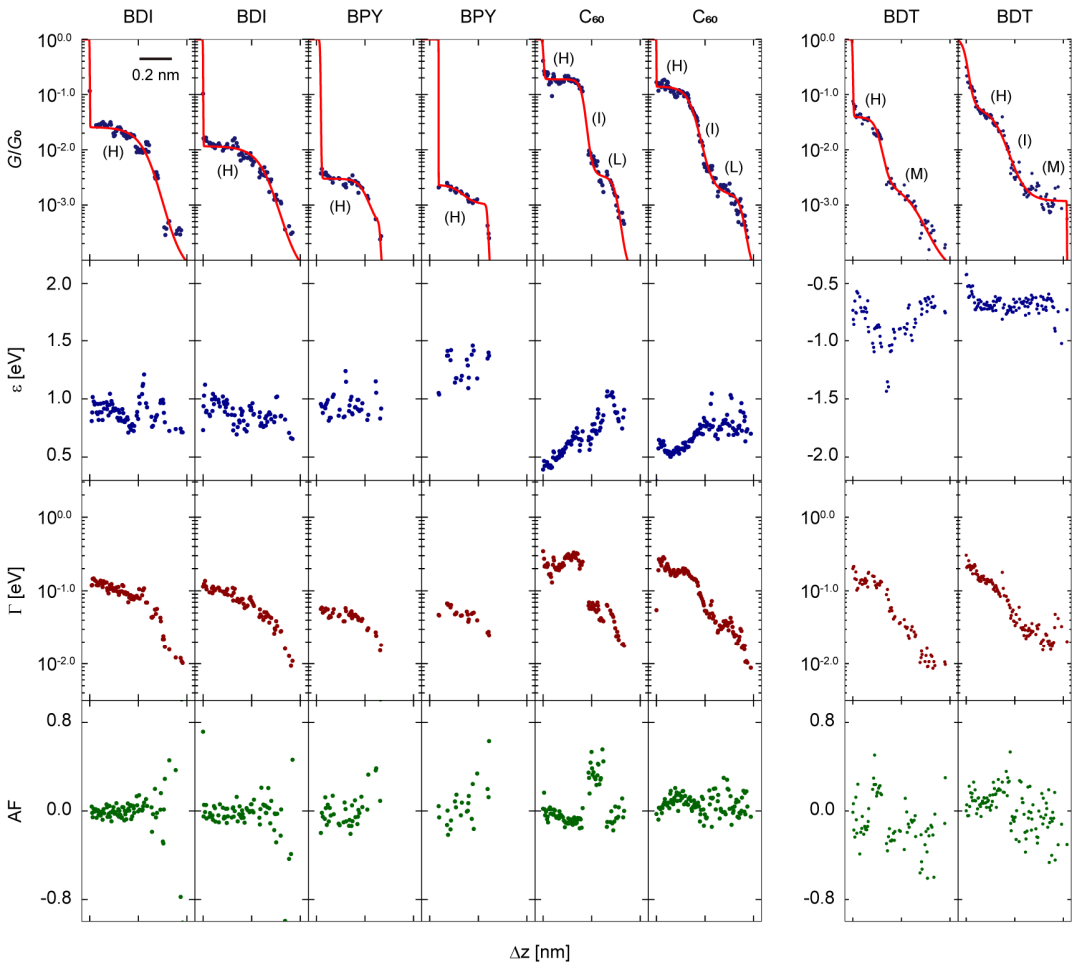

Fig. S7. *G*, *ε*, *Γ*, and AF plotted as a function of the junction-stretching distance (Δ*z*) for BDI, BPY, C_{60}, and BDT.

***I–V* measurements of *p*-phenylenediamine:**

We also measured *I–V* curves of *p*-phenylenediamine (PPD) during the junction stretching. PPD (Wako Pure Chemical Industries Japan, purity > 97.0%) was deposited on the Au(111) electrode by immersing the substrate in a 1 mM ethanol solution of each molecule for 3 hours. Fig. S7 shows the examples of ε and Γ with conductance plateaus in the range of $3 < G < 30$ mG_0 [S1, S2]. The $\partial \log G/\partial z$, $\partial \varepsilon/\partial z$ and $\partial \log \Gamma/\partial z$ values are summarized in Table S2. In PPD junctions, the total number of traces with conductance plateaus was 61 out of 5859 and enough data could not be obtained for statistical analysis. PPD exhibits 1/3 weaker molecule-Au bond than that of thiol molecules, which results in lower mechanical stability of the junction [S2, S3]. Conductance plateaus show that Δz in the H state is short, less than 0.2 nm. The number of data points is not enough to perform statistical analysis of which *I–V* curves for PPD.

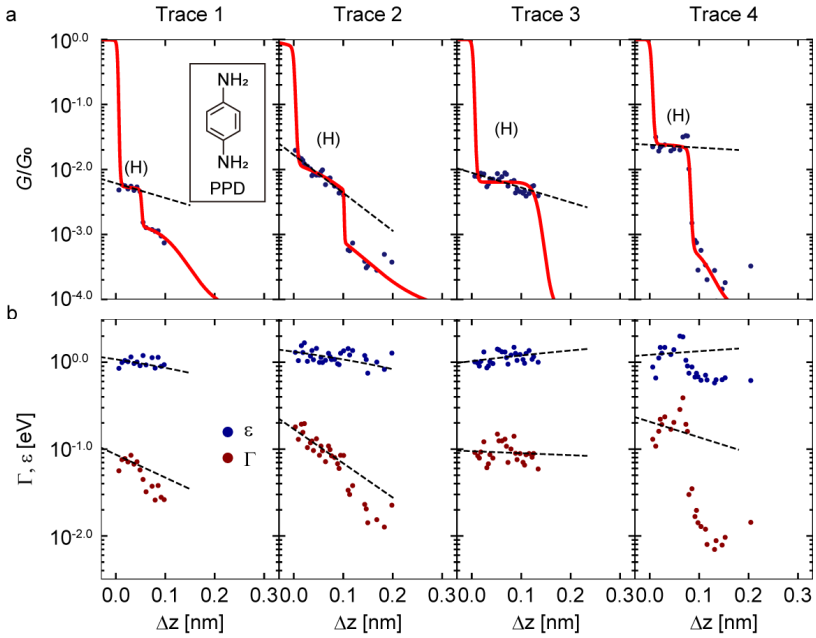

Fig. S8. Examples of (a) G, (b) ε, and Γ traces with respect to the junction-stretching distance. The dotted lines are the results of liner fitting.

	Trace 1	Trace 2	Trace 3	Trace 4
$\partial \log G/\partial z$ [nm^{-1}]	−2.25	−5.83	−2.28	−0.44
$\partial \varepsilon/\partial z$ [eV/nm]	−2.18	−2.44	1.68	1.21
$\partial \log \Gamma/\partial z$ [nm^{-1}]	−2.64	−3.94	−0.23	−1.79

Table S3. List of $\partial \log G/\partial z$, $\partial \varepsilon/\partial z$ and $\partial \log \Gamma/\partial z$ values of H states for the traces of Fig. S7.

Fitting to sigmoid functions and rate of change in G, ε and Γ with respect to Δz:

Stretching the single-molecule junctions results in a stepwise change in conductance traces (G–Δz traces), which correlate with the formation, evolution, breakdown, or transitions of the conduction states of the junctions.

First, the conduction states occurring in the G–Δz traces in Fig. 1d were analysed by fitting the following step-like sigmoid functions (equation (S2)) to the G–Δz traces.

$$\log_{10}\left(\frac{G(\Delta z)}{G_0}\right) = \sum_{i=1}^{N} \frac{A_i}{1+\exp\left(S_i(\Delta z - P_i)\right)} + C \qquad \text{(S2)}$$

where N is the number of functions, A_i is the amplitude, S_i is the slope, P_i is the central position of the function, and C is the offset. For details of the fitting procedure based on the sigmoid functions, see ref [S4]. Upper and lower limits of the total sigmoid function were set to $10^{0.0}\,G_0$ and $10^{-5.0}\,G_0$ respectively. N = 2 was used for BDI, N = 3 for BDT and C_{60}, and N = 4 for BPY. The dashed lines in Fig. S8 show individual fitted sigmoid functions ($s_1(\Delta z)$, $s_2(\Delta z)$, $s_3(\Delta z)$, and $s_4(\Delta z)$). For BDI and BPY, s_2 correspond to the H states. For BDT and C_{60}, s_2 and s_3 correspond to the H and M (or L) states, respectively (see also Fig. 1d).

Next, the rate of the change in G, ε, and Γ with respect to Δz (*i.e.*, $\partial \log G/\partial z$, $\partial\varepsilon/\partial z$, and $\partial \log\Gamma/\partial z$) were evaluated by linear fitting for the H, M, and L states, and the intermediate (I) states between and H and M (or L) states (Tables 1 and 2). The fitting ranges of $\partial \log G/\partial z$, $\partial\varepsilon/\partial z$, and $\partial log\Gamma/\partial z$ in the G–Δz, ε–Δz, and Γ–Δz traces (Fig. 1d) were determined based on the fitted sigmoid function (s_2) for BDI and BPY. The fitting range was defined as the range of $\Delta z < P_{i+1} - \ln 4/S_{i+1}$ where the amplitude of each sigmoid function is more than 80% of its maximum value. Considering scattered data points in the ε–Δz traces (Fig. 1d), data points showing large discontinuities with a difference between adjacent data points in ε greater than 0.1 eV were excluded from the G, ε, and Γ data sets when fitting the straight line. For BPY, the rate of change of ε and Γ as well as G was not evaluated because of the small number of data points in the L state in the G–Δz trace. In contrast to BDI and BPY, BDT and C_{60} showed the multiple conductance states and the clear transitions between them, and then evaluation ranges of the multiple conduction states and the intermediate state was defined by the following procedure. First, initial ranges of the conduction states and intermediate states were established based on the result of the fitted sigmoid functions (s_2 and s_3). Four ranges were used in BDT: Δz < 0.10 nm, 0.10 < Δz < 0.17 nm, 0.25 < Δz < 0.32 nm, and 0.32 < Δz < 0.40 nm because the change in G in the I state showed nonmonotonic behaviour. Three ranges were used in C_{60}: Δz < 0.23 nm, 0.23 < Δz < 0.38 nm, and 0.38 < Δz < 0.60 nm. Next, for each range, G–Δz trace, ε–Δz trace, and Γ–Δz traces (see Fig. 1d) were linearly fitted and the mean square error (MSE) was calculated for G, ε, and Γ (*i.e.*, MSE_G, MSE_ε, and MSE_Γ). Finally, while changing the width of the range, we found the region where $MSE_{total} = MSE_G \cdot MSE_\varepsilon \cdot MSE_\Gamma$ showed a minimum value and determined it as the region of the conductance and intermediate states.

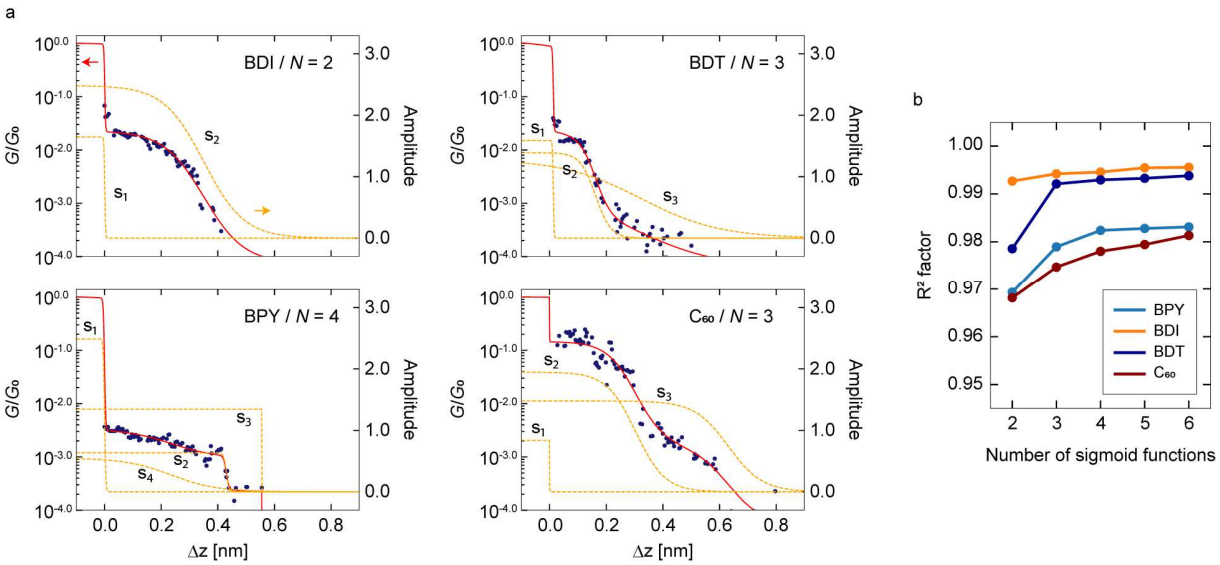

Fig. S9. G–Δz traces fitted with sigmoid functions for (a) BDI, (b) BPY, (c) BDT, and (d) C_{60} in Fig. 1d. Solid and dotted lines indicate the total and individual fitted lines. (e) Plot of the R^2 factor as a function of N for the fitting of equation (S2) to the G–Δz traces in (a)-(d). There was no significant difference in the shape of the fitted total sigmoid function with $N \geq 3$.

4. Statistical analysis of *I*–*V* curves

In 2D histograms, the x-bin size is 12 pm and the y-bin size is 0.02, 7.5 meV, 0.02 and 0.01 for G, ε, Γ and AF respectively. The bin size of 1D histograms is 0.08, 30 meV and 0.08 for G, ε and Γ. For 1D and 2D of ε, Γ, and AF, *I*–*V* datasets with $R^2 < 0.5$, $G > 0.0002\ G_0$ and $0.1 < \alpha < 0.9$ were used. $\partial \log G/\partial z$, $\partial \varepsilon/\partial z$ and $\partial \log \Gamma/\partial z$ were evaluated from peak values of 1D with respect to Δz (blue and orange markers in Figs. S10–S13b). As linear fitting ranges of $\partial \log G/\partial z$, $\partial \varepsilon/\partial z$ and $\partial \log \Gamma/\partial z$, $\Delta z < 0.39$, 0.20, 0.12 and 0.18 nm were used for H states of BDI, BPY, BDT and C_{60} and $0.12 < \Delta z < 0.30$ nm and $0.18 < \Delta z < 0.35$ nm were used for I states of BDT and C_{60} in which all three parameters are linearly changed. Here note that L state of C_{60} was seen at the close conductance range to I state at the range of $10^{-3} < G < 10^{-2}\ G_0$, which makes distribution of L states ambiguous in ε and Γ.

<u>Statistical analysis of *G*, *ε*, and *Γ* for BDI:</u>

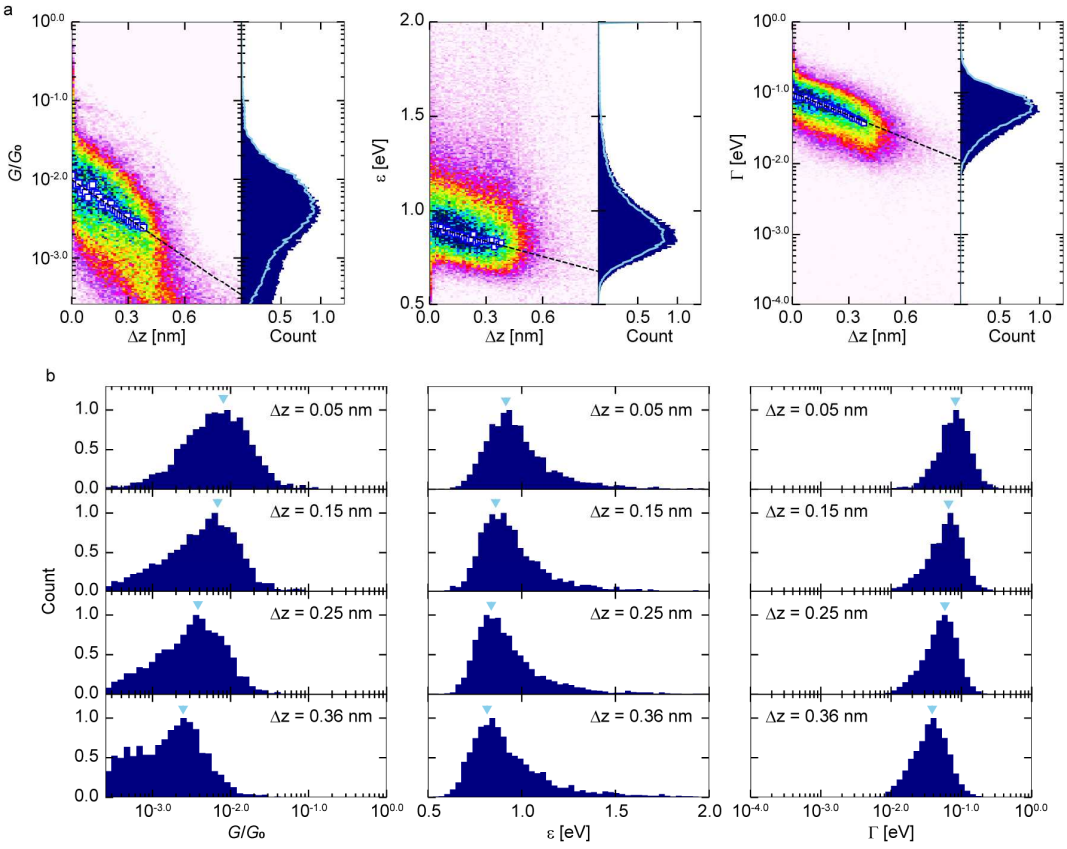

Fig. S10. Statistical analysis of G, ε, and Γ for BDI. (a) 2D histograms of $\log G$–Δz, ε–Δz, and $\log \Gamma$–Δz traces and 1D histograms of $\log G$, ε, and $\log \Gamma$. The 1D histogram of the H states (blue lines) are compiled using dataset with $\Delta z < 0.39$ nm. (b) 1D histograms of $\log G$, ε, and $\log \Gamma$ at several Δz points. Peak positions of H states are indicated by blue triangles.

Statistical analysis of G, ε, and Γ for BPY:

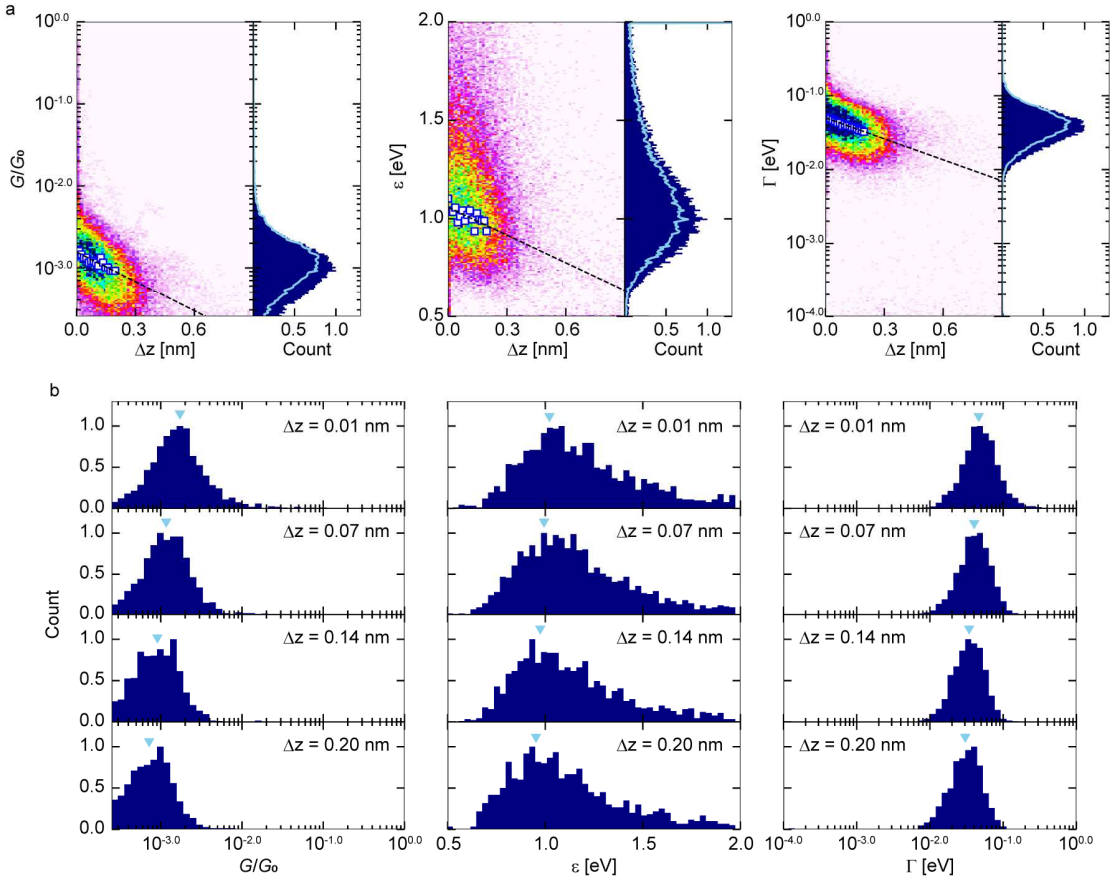

Fig. S11. Statistical analysis of G, ε, and Γ for BPY. (a) 2D histograms of log$G$–Δz, ε–Δz, and logΓ–Δz traces and 1D histograms of log$G$, ε, and logΓ. The 1D histogram of the H states (blue lines) are compiled using dataset with Δz < 0.20 nm. (b) 1D histograms of log$G$, ε, and logΓ at several Δz points. Peak positions of the H state are indicated by triangles.

Statistical analysis of G, ε, and Γ for BDT:

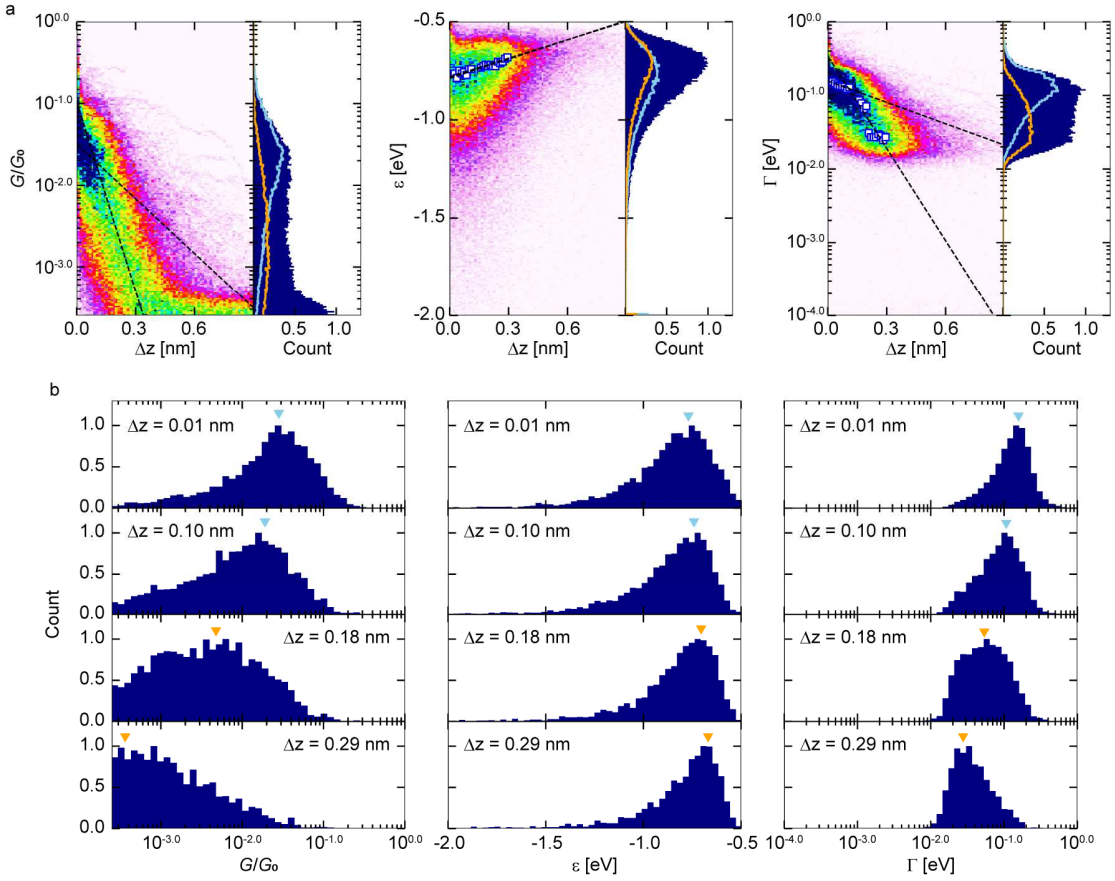

Fig. S12. Statistical analysis of G, ε, and Γ for BDT. (a) 2D histograms of log$G$–Δz, ε–Δz, and logΓ–Δz traces and 1D histograms of log$G$, ε, and logΓ. The 1D histograms are decomposed into two groups of the H and I states using a dataset with Δz < 0.12 nm (blue line) and 0.12 < Δz <0.30 nm (orange line). (b) 1D histograms of log$G$, ε, and logΓ at several Δz points. Peak positions of the H and I states are indicated by red and orange triangles respectively.

Statistical analysis of G, ε, and Γ for C_{60}:

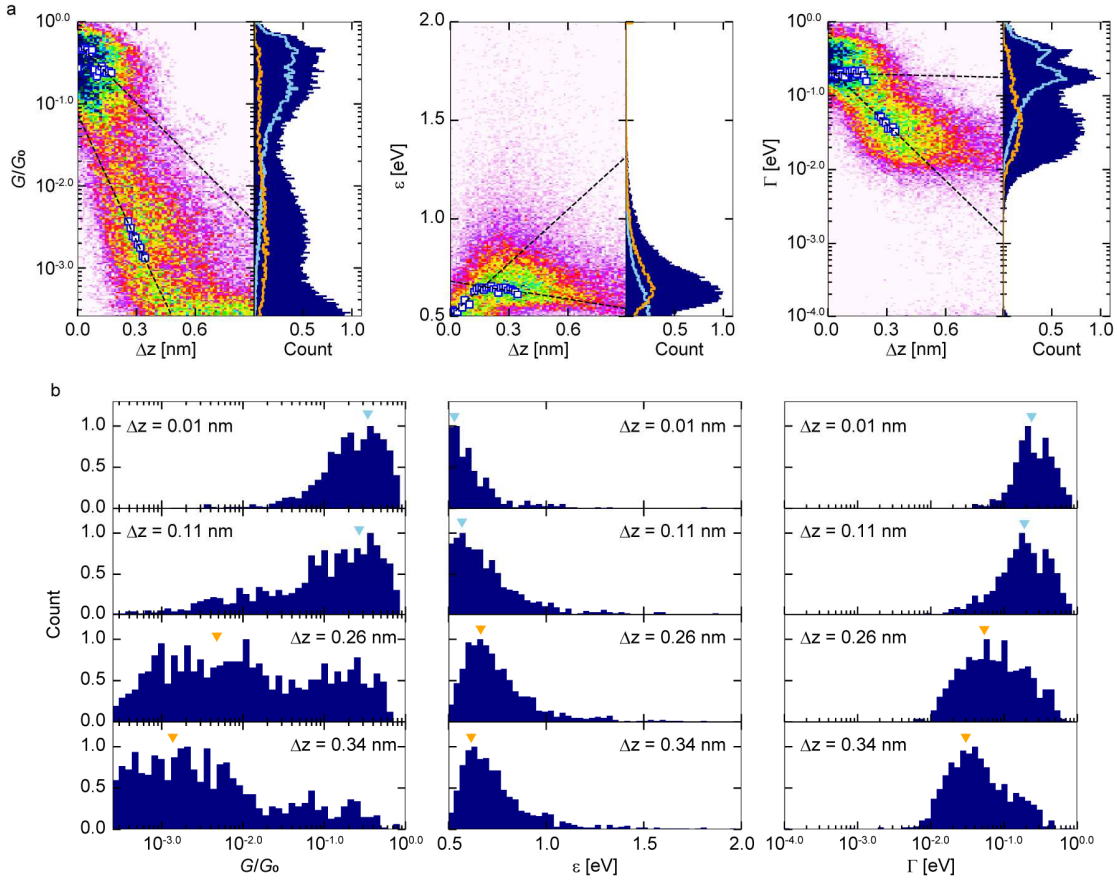

Fig. S13. Statistical analysis of G, ε, and Γ for C_{60}. (a) 2D histograms of log$G$–Δz, ε–Δz, and logΓ–Δz traces and 1D histograms of log$G$, ε, and logΓ. The 1D histograms are decomposed into two groups of the H and I states using a dataset with Δz < 0.18 nm (blue line) and 0.18 < Δz <0.35 nm (orange line). (b) 1D histograms of log$G$, ε, and logΓ at several Δz points.

Statistical analysis of AF for BPY, BDI, BDT, and C_{60}:

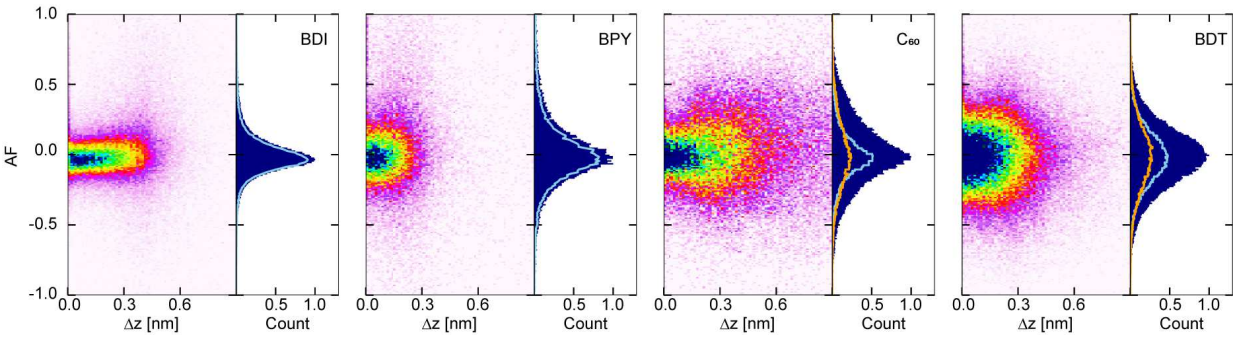

Fig. S14. Statistical analysis of AF. 2D and 1D histograms of AF–Δz traces for BDI, BPY, BDT and C_{60}. Blue and orange histograms correspond with H and I states.

Statistical analysis of $\partial\varepsilon/\partial z$ and $\partial \log\Gamma/\partial z$ for individual traces:

To evaluate the $\partial\varepsilon/\partial z$ and $\partial\log\Gamma/\partial z$ for the individual ε–Δz and Γ–Δz traces, each trace was divided into two or three segments and fitted with straight lines (Equation S3).

$$y_n = \begin{cases} a_0 \Delta z + b_0 & if\ n = 0 \\ a_n \Delta z + b_0 + \sum_{i=1}^{n} (a_{i-1} - a_i) k_i & if\ n \geq 1 \end{cases} \quad \text{(S3)}$$

n is the number of the segment and a_i is the slope of i^{th} lines and k_i is the boundary point shared between the adjacent fitting segments. The linear fitting was perfumed simultaneously for all pair of ε–Δz and Γ–Δz traces. n=1 was used for BDI and BPY, and n=2 was used for BDT and C_{60}. Compiling thousands of values obtained from a fitting range of more than 0.1 nm, 2D histograms of $\partial\varepsilon/\partial$z–Δ$z$ and $\partial\log\Gamma/\partial$z–Δ$z$ were created. The distributions were fitted with bivariate Gaussian distribution (equation S4):

$$z = \exp\left(-\frac{\left((x - x_0)sin\varphi - (y - y_0)cos\varphi\right)^2}{2\sigma_\varepsilon^2} - \frac{\left((x - x_0)cos\varphi + (y - y_0)sin\varphi\right)^2}{2\sigma_\Gamma^2} \right) \quad \text{(S4)}$$

x_0 and y_0 are centre of distribution and σ_ε and σ_Γ are standard deviation of $\partial\varepsilon/\partial$z and $\partial\log\Gamma/\partial$z. φ is the rotation angle (see in Fig. S16). C_{60} and BDT. Rotational angles of the distributions are φ = 9, 72, 0 and 27 degrees for BDI, BPY, C_{60} and BDT respectively.

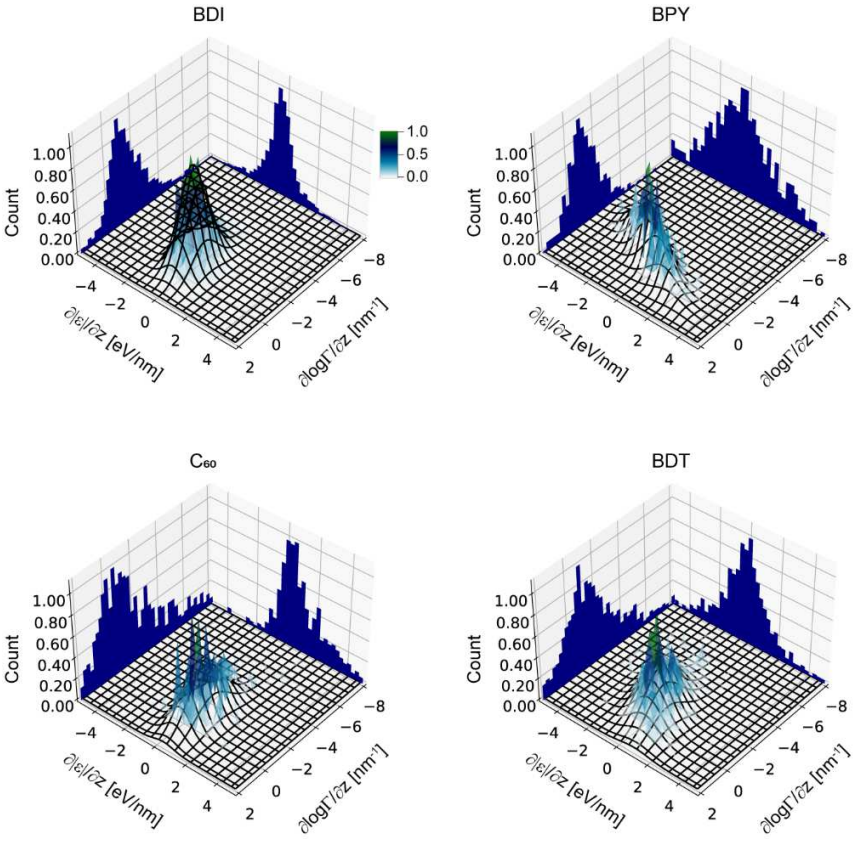

Fig. S15. Fitting results of 2D histograms with bivariate Gaussian distribution and 1D histograms of $\partial\varepsilon/\partial z$ and $\partial\log\Gamma/\partial z$ of BDI, BPY, C_{60} and BDT. Black mesh is the Gaussian distribution.

5. Statistical analysis of junction length

Fig. S16 shows length histograms of SMJs, which were constructed from G–Δz traces used for the creation of the histograms in Figs. S10–S13. For BPY and C_{60}, the length of the SMJs has been determined in a conventional standard BJ experiment under a constant low bias voltage of 100 mV.[S5] Distribution in length histograms is in good agreement between the previous study where the applied bias voltage was kept constant[S5] and the current study where the bias voltage was cycled at a high speed of kHz. These results suggest that similar junction morphology develops when SMJs are stretched with or without bias voltage cycling.

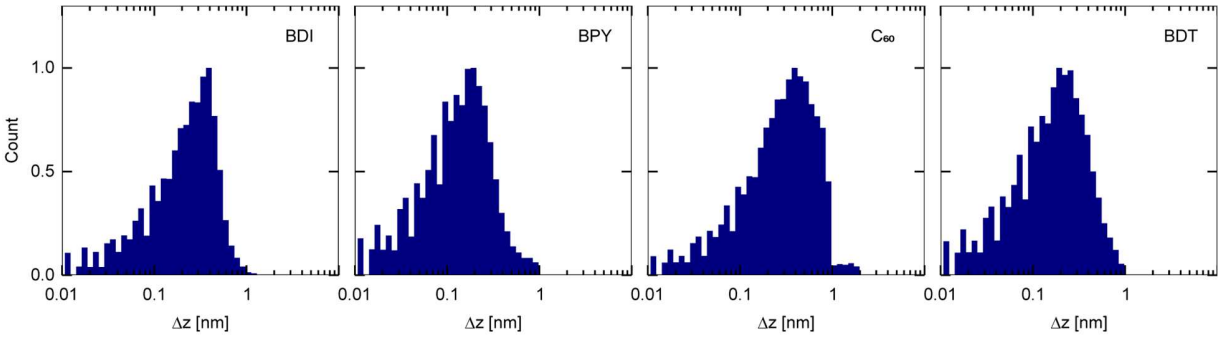

Fig. S16. Logarithmically binned length histograms of G–Δz traces for BDI, BPY, C_{60}, and BDT. Bin size of Δlog(Length/nm) is 0.06.

6. Calculated transmission spectra

Fig. S17 shows the calculated transmission spectra of Fig. 3a replotted over an extended energy range, where both occupied and empty resonances are visible. The data of Fig. 3a are replotted here for clarity.

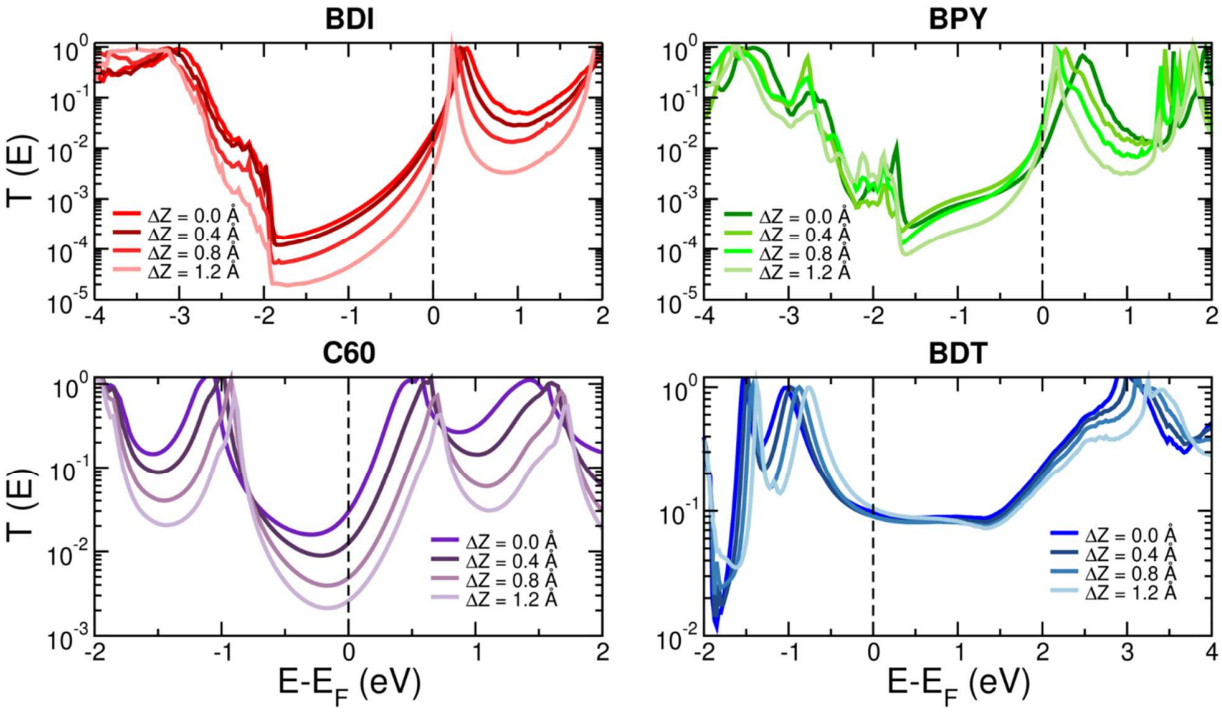

Fig. S17. Transmission spectra of Fig. 3a replotted over a wider energy range

7. Calculated junction geometries

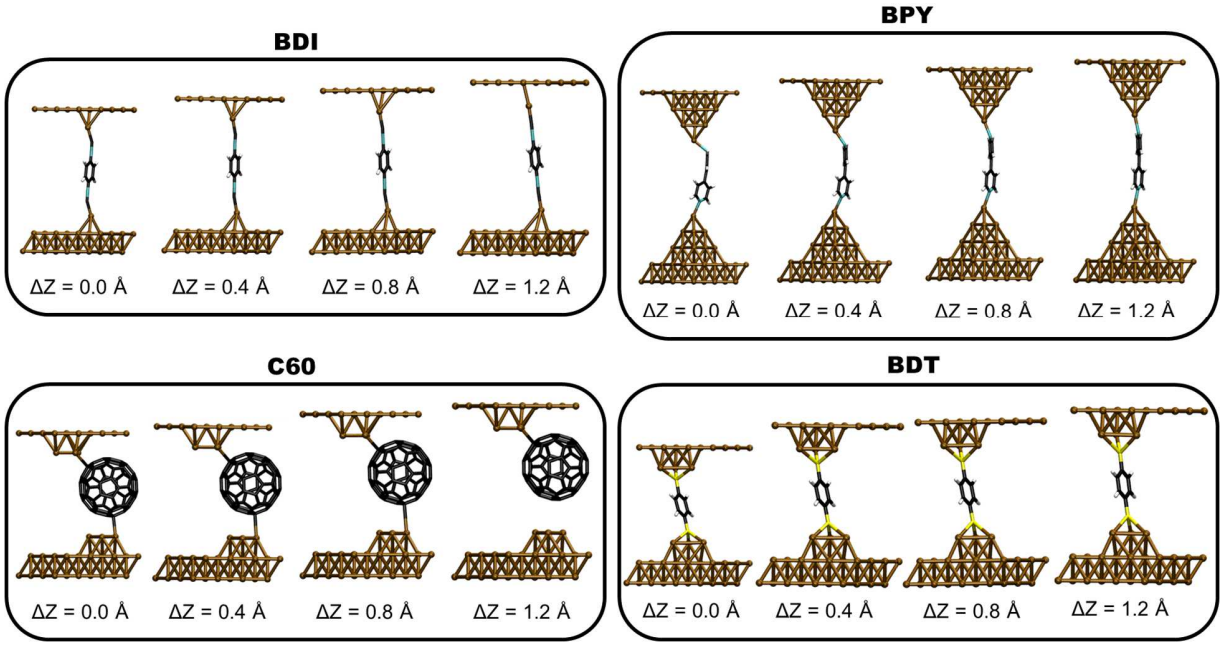

Fig. S18. Calculated junction geometries at different electrode separations

7. References

[S1] L. Venkataraman, J. E. Klare, C. Nuckolls, M. S. Hybertsen, M. L. Steigerwald, Dependence of Single-Molecule Junction Conductance on Molecular Conformation, *Nature* 2006, **442**, 904–907.

[S2] M. Frei, S. V. Aradhya, M. Koentopp, M. S. Hybertsen, L. Venkataraman, Mechanics and Chemistry: Single Molecule Bond Rupture Forces Correlate with Molecular Backbone Structure, *Nano Lett.* 2011, **11**, 1518–1523.

[S3] B. Q. Xu, X. Y. Xiao, N. J. Tao, Measurements of Single-Molecule Electromechanical Properties, *J. Am. Chem. Soc.* 2003, **125**, 16164–16165.

[S4] Y. Isshiki, T. Nishino, S. Fujii, Electronic Structure and Transport Properties of Single-Molecule Junctions with Different Sizes of π-Conjugated System, *J. Phys. Chem. C* 2021, **125**, 3472–3479.

[S5] Y. Isshiki, S. Fujii, T. Nishino and M. Kiguchi, Fluctuation in Interface and Electronic Structure of Single-Molecule Junctions Investigated by Current versus Bias Voltage Characteristics, *J. Am. Chem. Soc.*, 2018, **140**, 3760–3767.